

COMPUTER SIMULATION STUDIES
OF COMPENSATION OF TURBULENCE DEGRADED IMAGES*

Benjamin L. McGlamery
Visibility Laboratory
Scripps Institution of Oceanography
University of California, San Diego
San Diego, California 92093

Abstract

Techniques have been developed which allow nearly all phases of the image forming process for turbulence degraded images to be computer simulated. The simulation includes generation of turbulence degraded wavefronts, the degrading point spread function, and the sensor properties. Pre detection compensation of the wavefront and post detection compensation of the image can likewise be simulated. These simulation techniques have been used to determine fundamental limits of pre detection and post detection processing. Results of the application of these techniques to sun-illuminated objects will be presented in this paper.

Introduction

The random spatial and temporal variations of the index of refraction of the earth's atmosphere severely limits the resolution of large diameter ground based telescopes. For example the diffraction limit of a perfect 1.5 meter lens in the absence of the atmosphere is on the order of .1 arc seconds (radius of the Airy disk) at $\lambda = 550$ nanometers. With the earth's atmosphere present, star images very seldom reach this limit. Instead star images on the order of one arc second are typically observed. Removal of this resolution-limiting degradation is a subject of great interest to the various disciplines concerned with photographing celestial objects from ground based locations.

Several approaches exist. One approach is post detection processing in which the image is recorded in degraded form, then scanned, digitized, and processed in a digital computer to enhance information extraction from the image. This approach has been under investigation for many years but, as will be demonstrated here, is limited because the signal to noise ratio in the degraded image usually does not permit a significant improvement in resolution.

A more promising approach currently under development in several laboratories is pre detection compensation using an active optical system which, in real time, senses the wavefront deformations introduced by the atmosphere, and corrects these deformations by means of a deformable mirror so that the recorded image is largely free from degradation.

In both post and pre detection compensation the ultimate goal is to increase the amount of information which can be extracted from an object. In some cases it is difficult to formulate an image quality parameter which can measure the increase in image information extraction based on the optical system alone. This is because the improvement in image quality depends on the nature of the object itself and on the kind of information that is to be extracted from the image.

An approach to the problem of analyzing compensated imaging systems performance is by computer simulation of the final image that would be formed by the system. Assessment of image quality improvement can then be made on the basis of analyzing this image in terms of the particular kind of information that is desired from it. In addition the simulation approach is useful for verifying results of analysis and for optimizing system design in those cases where tractable analytical models cannot be formulated.

This paper will present the procedures used in simulating both pre and post compensated images recorded through the turbulent atmosphere and will show examples of these procedures.

Simulation of Atmospheric Effects

Wavefront Simulation

Simulation of the wavefront entering the optical system is a key element of the overall simulation approach. Given the wavefront or wavefronts, the response to the wavefront by the optical system can then be computed.

* The research work leading to this paper was performed under ARPA Contract No. F30602-76-C-0027.

Consider a point source at a great distance from the earth so that a wave entering the atmosphere can be considered to be a plane wave. After traversing through the atmosphere the wave will no longer be plane but will have an amplitude and phase distribution across the lens. In this paper we will consider only phase distribution since the phase variations across the wavefront are the dominant image degrading component.

One way of describing the phase statistically is by means of its power spectrum. For atmospheric turbulence a spatial power spectrum, Φ , commonly used is the Kolmogorov spectrum which has the form of

$$\Phi(f) = Cf^{-11/3} \quad (1)$$

where

f = spatial frequency, cycles/meter.

C = is a constant dependent upon turbulence strength and wavelength.

The method of generating an instantaneous phase map using the above power spectrum is based on the following assumptions:

- 1) The modulus of the Fourier transform of the phase map is a random variable. At any given frequency the modulus is a Rayleigh random variable with zero mean over an ensemble average and with a variance, over an ensemble average, equal to the value of the Kolmogorov power spectrum.
- 2) The phases of the Fourier transform of the phase map are independent with frequency, uniformly randomly distributed in the $-\pi$ to $+\pi$ interval.

Based on these assumptions the following procedure is used to generate the phase map.

1. A complex array of Gaussian random numbers is generated. The array represents the spatial frequency domain for the phase map.
2. The array is multiplied by the square root of the power spectrum, $f^{-11/6}$ (since we are at this point working with amplitudes rather than power).
3. This array is subjected to a discrete Fourier transform.
4. The resulting complex array is separated into its real and imaginary components. Each of these arrays represent an independent instantaneous phase map realization.

Figure 1 shows the result of the above process for three separate realizations. It is interesting to note that the phase maps have a cloud-like appearance.

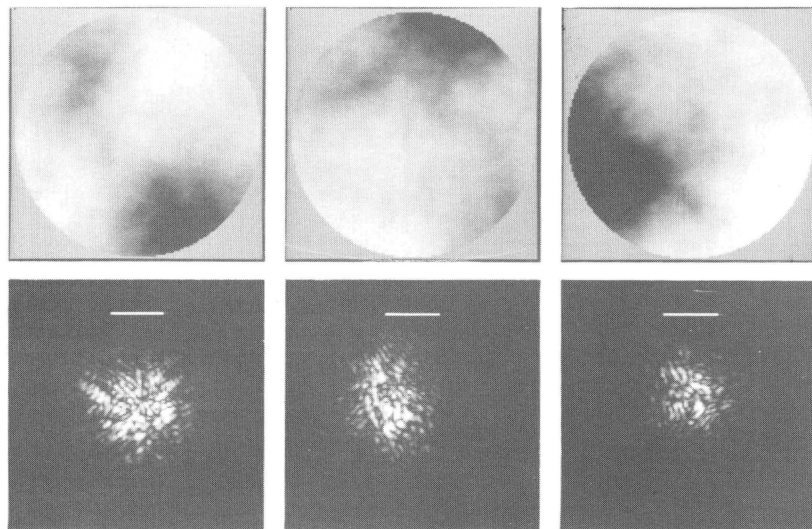


Fig. 1. Top row: phase maps. Bottom row: associated point spread functions for $r_o = .1$ meter, pupil diameter = 1.5 meters, $\lambda = 550$ nanometers. The bar indicates one arc second.

Another statistical parameter associated with the phase map is its structure function, defined as

$$D_{\phi}(r) = \langle \phi(r') - \phi(r'+r) \rangle^2 . \quad (2)$$

The structure function is the ensemble variance of the phase difference between two points on the wave-front separated by the vector r . In a medium with uniformly varying refractive index structure constant, C_n^2 , the Kolmogorov spectrum can be shown to have a phase structure function of⁽¹⁾

$$D_{\phi}(r) = 2.91k^2 r^{5/3} \int C_n^2(z) dz \text{ (radians}^2\text{).} \quad (3)$$

The conditions of validity of this equation are $r \gtrsim \sqrt{\lambda H}$ and $\sqrt{\lambda H} \gg \ell_o$ where ℓ_o is the inner scale of the turbulence.

The structure function can be written as

$$D_{\phi}(r) = 6.88 \left(\frac{r}{r_o} \right)^{5/3} \quad (4)$$

where $r_o = [6.88 / 2.91 k^2 \int C_n^2(z) dz]^{3/5}$. The parameter r_o is a length frequently used to characterize the strength of atmospheric turbulence with respect to the performance of optical systems. A median value of r_o for night time seeing has been computed to be on the order of .1 meters.⁽²⁾

The structure function $D_{\phi}(r)$ and the covariance function $C_{\phi}(r)$ of a phase map can easily be shown to be related by

$$D_{\phi}(r) = 2 [C_{\phi}(0) - C_{\phi}(r)], \quad (5)$$

where the covariance is defined as

$$C_{\phi}(r) = \langle C_{\phi}(r') C_{\phi}(r'+r) \rangle . \quad (6)$$

The covariance function is also the Fourier transform of the power spectrum of the phase map. Thus by applying the discrete Fourier transform to the phase power spectrum, the phase structure function can be computed by use of Eq. (5). When this is done using the discrete Fourier transform one finds that the structure function for simulated phase maps follows the theoretical 5/3 law of Eq. (4) only for very small separations. Let L be the interval in space represented by the discrete Fourier transform. For $r/L = .05$ D_{ϕ} is 10% lower than the true value. For $r/L = .1$ D_{ϕ} is 20% lower than the true value and the slope of the log-log plot of D_{ϕ} versus r/L is rapidly decreasing below the 5/3 value. This is due to the fact that the Kolmogorov spectrum assumes an infinite outer scale while the method of generating the phase maps imposes an artificial outer scale of L , since no frequencies lower than $1/L$ exist in the Fourier transform.

The outer scale of L imposed by the discrete Fourier transform method can be shown to cause errors mainly in the average and tilt components of phase across the phase map. The average component is usually of no interest and the tilt component causes only a shift of the image formed by lens. We have determined that a phase map of $L/4 \times L/4$ (extracted from a $L \times L$ array) with piston and tilt removed has statistical properties which almost exactly match theoretical values. Thus the method of generating phase maps outlined is entirely adequate for those cases where overall tilt across the pupil is of no concern.

Point Spread Function Simulation

The point spread function is the irradiance distribution in the image plane of the telescope using a point source at infinity as an object. It is useful in simulating the image of an extended object in that if the object is incoherently illuminated and the point spread function is invariant over the angular field of view of the object, then the image can be simulated by convolving the point spread function with the radiance distribution of the object.

Let the (u, v) be the pupil plane coordinates and (x, y) the image plane coordinates. Given the instantaneous phase map at a wavelength of $\lambda, \phi(u, v, \lambda)$, we can compute the path length difference map, $\ell(u, v)$, from

$$\ell(u, v) = \frac{\phi(u, v, \lambda)}{2\pi} . \quad (7)$$

The coherent point spread function, $s(x, y, \lambda)$ at any wavelength can then be computed from

$$s(x, y, \lambda) = F \left\{ p(u, v) e^{i \frac{2\pi \ell(u, v)}{\lambda}} \right\}, \quad (8)$$

where F is the Fourier transform operation and $p(u, v)$ is the pupil function of the telescope. This step is based on the fact that under appropriate conditions (i.e. small angle conditions) there is a Fourier transform relationship for coherent light between the pupil plane and the image plane except for a quadratic phase factor.⁽³⁾ The quadratic phase factor is of no concern here since it is lost when the intensity point spread function $S(x, y)$, is computed from

$$S(x, y, \lambda) = |s(x, y, \lambda)|^2. \quad (9)$$

The point spread function for all wavelengths is then given by

$$S(x, y) = k_2 \sum_{\lambda} F(\lambda) S(x, y, \lambda), \quad (10)$$

where $F(\lambda)$ is a weighting function which is a product of the spectral distribution of the source power, the atmospheric transmittance and the image sensor sensitivity, and k_2 is a normalizing factor which makes the average value of $S(x, y)$ unity over the array. An additional factor not shown in Eq. (10) which must be considered in simulating the polychromatic point spread function is that the angular scale associated with $S(x, y, \lambda)$, as computed from Eqs. (8) and (9) using a discrete Fourier transform, changes with λ . Thus in Eq. (10) the $S(x, y, \lambda)$ arrays must be spatially magnified proportional to λ before the summation is performed.

Point spread functions for monochromatic light for three phase maps are shown in Fig. 1. The result of the generation of a polychromatic point spread function is demonstrated in Fig. 2.

Simulation of Degraded Images

As mentioned previously the degraded image which would be present in the image plane can be simulated by convolving the intensity point spread function with the radiance map of the undegraded object, subject to the conditions that the point spread function is invariant over the object and that the object is illuminated by incoherent light. Whether the first condition is satisfied depends on the relative size of the object and the isoplanatic region, the latter being a non rigorous term for the region over which the point spread function is nearly constant. The size of the isoplanatic region depends both on the vertical distribution of the turbulence and the entrance pupil diameter. For turbulence at the entrance pupil the isoplanatic region is unlimited. For turbulence at high altitudes (> ten kilometers) and a 1.5 meter entrance pupil diameter the isoplanatic region is on the order of ten arc seconds or less. The second condition of incoherent illumination is satisfied for sun illuminated objects.

The convolution process is mathematically described by Eq. (11) where $H(x, y)$ is the image plane irradiance in the absence of turbulence and diffraction and $H_D(x, y)$ is the degraded image,

$$H_D(x, y) = \iint H(x, y) S(x-x', y-y') dx' dy' \quad (11)$$

In practice the convolution process is more easily done in the Fourier transform domain:

$$H_D(x, y) = F^{-1} \{ F[H(x, y)] \cdot F[S(x, y)] \} \quad (12)$$

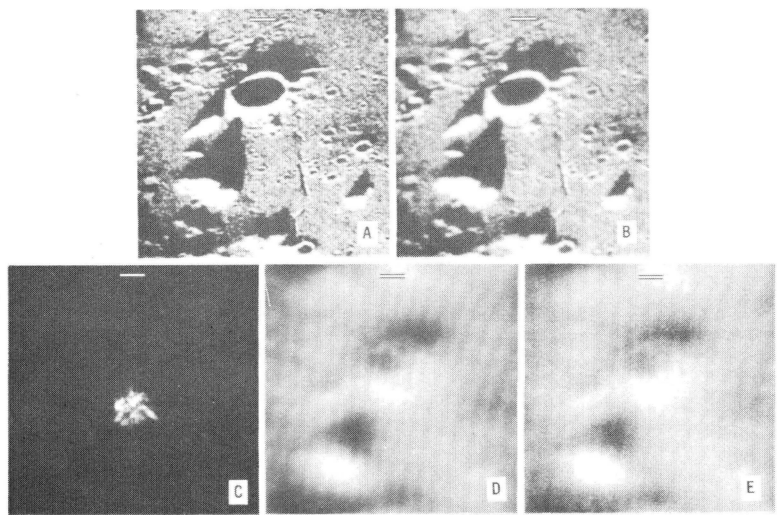
where F and F^{-1} are the Fourier transform and inverse transform operators.

In addition to the turbulence and telescope, the sensor also degrades the image. Ideally the sensor imposes only quantum noise on the recorded image. In practice the sensor sometimes additionally blurs the image and adds noise not directly related to the light field. However, suitable selection of the sensor these effects can be minimized. Here we assume that the sensor is ideal so that the recorded image, $H_R(x, y)$, can be expressed as $H_R(x, y) = H_D(x, y) + N(x, y)$ where $N(x, y)$ describes a noise array. For the ideal sensor $N(x, y)$ is a sample from a Poisson noise distribution which at any given (x, y) coordinate has a mean and variance proportional to $H_D(x, y)$.

Figure 2 illustrates the simulation of the degraded image. The object chosen for the simulation is a section of the moon's surface photographed from the Apollo 17 command module. The bar represents the distance subtended by a one arc second angle from the earth. Also shown is the appearance of the image due to diffraction of the telescope alone, the polychromatic point spread function (which includes telescope pupil effects) and the convolution of the undegraded image and the point spread function, which results in the degraded image. Finally the recorded image with sensor noise is shown. The noise has Poisson characteristics based on the mean number of photoelectrons per resolution element for: solar irradiance, a spectral atmospheric transmittance corresponding to one air mass, a telescope transmittance of .75, a sensor sensitivity corresponding to an S20 photocathode, an exposure time of 1/1000 second, and a 1.5 meter diameter telescope. In the picture the noise is easily not discernable. However, the noise is present and will manifest itself when image restoration techniques are applied.

Fig. 2. Computer simulation of an atmospherically degraded image. Bar indicates one arc second. 256x256 array.

- a) A portion of the Moon's surface from Apollo 17 photography.
- b) Simulated diffraction limited image from Earth-based telescope of 1.5 meter diameter, $\lambda = 550$ nanometers.
- c) Simulated polychromatic atmospheric point spread function.
- d) Degraded image formed by convolution of a) and c).
- e) Poisson noise added to d) for S(20) photocathode, 1/1000 second exposure.



Post Detection Processing

Post detection processing refers to processing done on an image after it has been recorded. The basic steps when digital computer processing is used consists of digitizing the image, applying the appropriate processing algorithms, and displaying the final result or data in some suitable form. Many possible approaches can be taken^(4, 5) but the one to be used here is the deconvolution approach in which the goal of the processing is to make the final image visually look like the object.⁽⁶⁾ Simply stated, given the degraded image and the point spread function, determine the undegraded image. This approach assumes that the instantaneous point spread function is known. While in practice it may be difficult to know the instantaneous point spread function, we will assume that it is known. The limitations to this approach, and in fact all approaches, is the quantum noise in the recorded image. This noise limits the extent to which the image can be deconvolved.

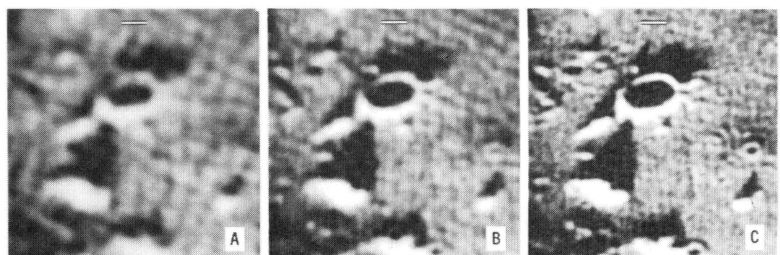
As an example, the degraded image of Fig. 2 has been subjected to a least squares processing algorithm⁽⁷⁾ modified to account for lack of knowledge of the spatial power spectrum of the undegraded image. The processed image, $H_p(x, y)$, is obtained from

$$H_p(x, y) = F^{-1} \left\{ \frac{F[H_D(x, y)]}{F[S(x, y)] \left[1 + \frac{\sigma^2(f_x, f_y)}{|F[S(x, y)]|^2 G(f_x, f_y)} \right]} \right\}$$

where σ^2 is the spatial noise power spectrum and G is a function which approximates the power spectrum of the undegraded image. Figure 3 shows the result of the processing. The processed image is improved over the degraded image but falls far short of the diffraction limited image. Also shown are the degraded and processed images for exposure times of 1/100 and 1/10 seconds. In each case the atmosphere is assumed to be frozen. In actuality the turbulence changes rapidly so that the 1/100 and 1/10 second exposures would contain time averaging of the image. Time averaging increases the degradation of the image. Thus the increase in image signal to noise ratio is offset by the increase in image degradation. This illustrates a fundamental limitation of post detection processing as applied to turbulence degraded, sun illuminated objects.

Fig. 3. Post detection processed images, using modified least squares filter and full knowledge of point spread function. Frozen atmosphere assumed.

- a) 1/1000 second exposure image processed.
- b) 1/100 second exposure image processed.
- c) 1/10 second exposure image processed.



Pre Detection Compensation Systems

An alternate approach to the problem of eliminating turbulent effects is to correct the wavefront prior to recording the image. This technique was suggested over twenty years ago⁽⁸⁾ but has received serious attention only recently. Theoretical analyses⁽⁹⁾ and computer simulations demonstrating concepts⁽¹⁰⁾ have been published. The contribution of this paper is to present simulations based on typical imagery and actual flux levels that will be encountered with sun illuminated objects.

System Description

Figure 4 shows the essential components of a pre detection compensation system. Light from the telescope objective is recollimated and reflected off a deformable corrector mirror. Part of this light is reflected into a wavefront sensor which detects the wavefront deformations introduced by the atmosphere. The output from the wavefront sensor is processed by a data processor which determines the necessary signals to be fed to the deformable mirror to cancel out the wavefront deformations. Thus the system is a closed loop servo system. The remaining flux is directed to the image sensor to form the final image.

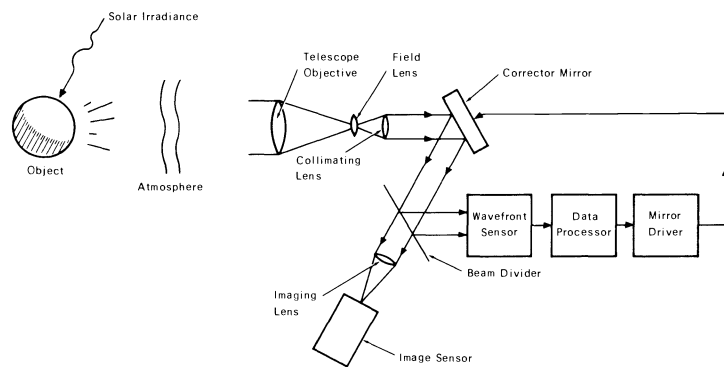


Fig. 4. Components of a pre detection compensated imaging system.

The wavefront sensor can be implemented in a variety of ways. Most approaches measure the slope of the wavefront over an array of sample points. The data processor then converts the slopes into the required phase corrections. The shearing interferometer and the quadrant detector appear to be two of the more promising wavefront sensors. The shearing interferometer⁽¹¹⁾ has two channels, one for u and the other for v, in which the wavefront is sheared and allowed to interfere with itself. An array of detectors measures the intensity of the interference field. The phase of the sheared wave is temporally modulated so that an alternating signal is obtained from each detector. The phase of this signal is proportional to the slope of the wavefront over the shear distance. The phase at each detector in both channels is measured, thus providing the necessary input to the data processor. The quadrant detector approach uses an array of small sub apertures at an image of the pupil plane (or at some point outside the telescope). Each sub aperture-diffraction limited image of the object, shifted by the slope of the wavefront across the sub aperture. The quadrant detector outputs allow this shift to be measured in both the u and v directions, thereby providing an estimate of the wavefront slope at that point.

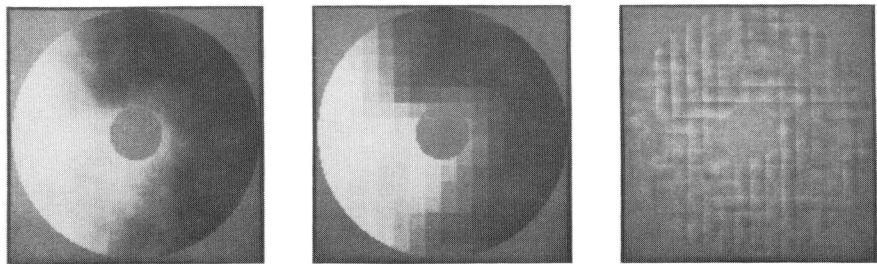
The data processor can take several forms. For the purpose of the simulations here, it will consist of a device which makes a simple least squares estimate of the wavefront path length differences based on the slope measurements.

The wavefront corrector can be a segmented mirror or a deformable mirror. In the case of a segmented mirror each segment can be moved in a piston motion, thus requiring one actuator per segment, or can be moved in piston and tilt, thus requiring 3 actuators per segment. In a deformable mirror the mirror is continuous but is actuated by piston type actuators. The continuous mirror provides an interpolation function which smooths out the inputs to the actuators. The shape of this interpolating function, called the mirror function, can be adjusted by design of the mirror, the actuator shape and spacing.

The effect of compensating a wavefront using a segmented mirror with piston drive is illustrated in Fig. 5. In this simulation it was assumed that the average phase over each piston element was known exactly and was subtracted from the original wavefront. The residual errors in the compensated wavefront are then due to the variations of the original wavefront about the mean value within each piston.

Fig. 5. Example of wavefront compensation using a segmented mirror.

- a) Phase map.
- b) Phase map represented by piston displacements.
- c) Residual wavefront, difference between a) and b).



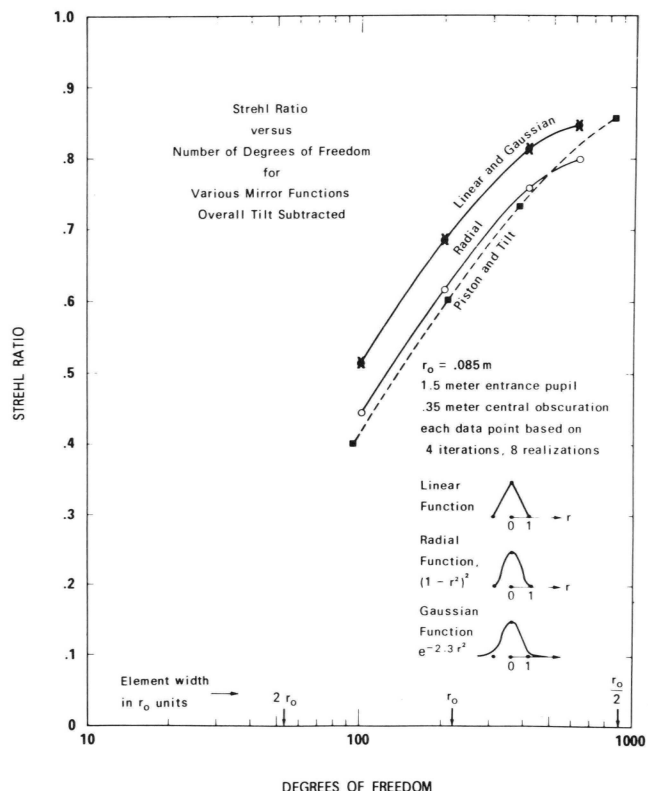
Number of Elements

A critical parameter in a compensated imaging system is the number of sample points and actuators required on the wavefront sensor and corrector. From the standpoint of being able to measure and correct the deformations of the wavefront with sufficient resolution, a large number of elements is desirable. To determine the number of elements required for good compensation, a computer simulation experiment was performed in which the Strehl ratio of the compensated point spread function was computed as a function of the number of degrees of freedom, which is the number of actuators required on the mirror. The Strehl ratio is the ratio of the peak value of the compensated point spread function to the peak value of the diffraction limited point spread function. A value of unity would correspond to perfect compensation. A value well below .1 is usually encountered in uncompensated point spread functions. The experiment was performed for an r_o of .086 meters. For the segmented mirror with piston correction the average phase over each segment was subtracted from the original wavefront. For the segmented mirror with piston and tilt correction a least squares fit of a plane was made to the phase within each segment and this plane was subtracted from the original wavefront over each segment. For the deformable mirror the average phase over a square equal to the actuator spacing was used as the correcting phase for the actuator, and the correction process was iterated four times to converge on the required correction. In all cases 8 different wavefront realizations were used to obtain a statistically significant result.

The results of the simulation are shown in Fig. 6 for piston and tilt, deformable mirror corrections. Assuming that a Strehl ratio of .7 is desired for good imagery and taking the value of r_o of .086 meters as being close to typical, the required number of degrees of freedom are:

Piston (not shown)	~ 900 degrees of freedom
Piston and Tilt	~ 300 degrees of freedom
Deformable Mirror	~ 200 degrees of freedom

Fig. 6. Strehl ratio versus degrees of freedom for piston and tilt and for a deformable mirror with various mirror functions.



These results show that a deformable mirror with a Gaussian mirror function requires the fewest number of elements for a given level of performance and that the number of elements required is on the order of several hundred.

The curves just described are related to the ability of the system to spatially resolve the wavefront deformations. They do not include measurement error of the wavefront sensor due to quantum noise. The output of a single detector in the wavefront sensor contains a signal proportional to wavefront slope and noise due to the shot effect of the photoelectrons. As the number of elements increases, the flux available for a single detector decreases. The signal to noise ratio at each detector then decreases as the number of elements increases. Thus these are two opposing trends: increasing the number of elements improves the ability to resolve the wavefront deformations but at the same time increases wavefront measurement error due to noise. Analysis has shown that for a given set of target and system conditions there is an optimum number of elements for which the error in the compensated wavefront is a minimum. The number of elements is in the range of 200 to 400 for typical sun illuminated objects.

Simulation

In order to demonstrate its effectiveness, a pre detection compensated imaging system has been computer simulated. The simulation used a shearing interferometer as wavefront sensor and a deformable mirror with a $(1 - ar^2)^2$ mirror function. The simulation consisted of the following steps:

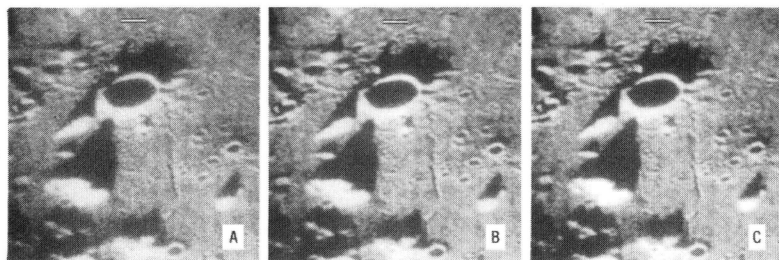
1. Shifting and differencing the wavefront in u and v and sampling the result to obtain u and v arrays of shear values.
2. Computing the actuator drives from the shear values by use of an iterative relaxation algorithm which computes phase values from the shear values.
3. Convolving the actuator drives with the mirror function to give the mirror correction.
4. Subtracting the mirror correction from the original wavefront to give the corrected wavefront.
5. Using the corrected wavefront as an input to step 1 and repeating the steps 1 through 4 for 4 iterations. This procedure is necessary to get the system initially converged.
6. Adding noise to the converged wavefront slopes by an amount obtained from a signal to noise equation. The noise is a function of the number of photoelectrons generated at the detector in a measurement period and the mutual coherence function associated with the object. The noisy shear values were then used as the input to step 2 and steps 2, 3 and 4 were repeated.
7. The corrected wavefront from step 4 was then used to compute the compensated point spread function.
8. The compensated point spread function was convolved with the undegraded image.
9. Poisson shot noise was added to the final image in proportion to the amount of flux directed towards the sensor by the beam divider.

Parameters used in the simulations are as follows. Object: sun illuminated Lunar surface with the photometric parameters adjusted to give an albedo (reflectance) of approximately 10% on the planes and 30% on the crater edges; atmospheric transmittance associated with one air mass; telescope transmittance of .75, optical efficiency of wavefront sensor of 50% (25% into each channel); quantum efficiency of detectors of 10%; and a 50/50 beam divider.

The results of the simulation are shown in Fig. 7 for exposure times of 1/1000, 1/100, and 1/10 of a second assuming a frozen atmosphere. As in the case of post detection processing, caution must be used in interpreting the results for 1/100 and 1/10 second since the atmosphere may change in this time period. Comparison to the post detection processing results in Fig. 3 demonstrates that pre detection compensation produces a much better image for the equivalent exposure time.

Fig. 7. Pre detection compensated images. Number of elements in 1.5 meter diameter clear aperture = 304. $r_o = .1$ meter. Shearing interferometer used for wavefront sensor, deformable mirror with radial mirror function used for corrector. Frozen atmosphere assumed. 256x256 array.

- a) 1/1000 second exposure.
- b) 1/100 second exposure.
- c) 1/10 second exposure.



Limitations

Several factors will place limitations on the application of pre compensation systems. The problem of isoplanatism has not been discussed with respect to pre detection compensation. The isoplanatic region for pre detection compensation may be much smaller than for post detection compensation. The manner in which the limited isoplanatic region can be extended is unresolved at the present and is a subject for consideration in the design for a pre compensated system. Low flux levels is another limitation. The wavefront compensation must be done at rates which match the atmospheric time constant. If the wavefront sensor does not obtain enough flux in this time interval, then the system will not function. This precludes long time exposures on dim objects such as galaxies and nebula. However, if a bright star exists within the isoplanatic region then by means of a field stop, this star could be used to drive the wavefront sensor. Calculations indicate that a sixth or seventh visual magnitude star would supply sufficient flux for the wavefront sensor. A long time exposure could then be used to photograph the dim object.

Conclusions

Computer simulation is a useful technique for analysis of turbulence degraded wavefronts and their effect on the images formed by optical systems. The simulations shown here demonstrate the potential advantage of pre compensating the wavefront prior to recording the image as opposed to post detection correction of the image itself. Since the same amount of flux is available in both cases, the result implies that useful information is irretrievably lost in the recording process. Presumably this lost information is associated with the electromagnetic phase correlations induced in the image of the atmosphere which are lost in the recording process.

Acknowledgements

The author is indebted to Dr. Donald Silva for providing the pre compensated wavefronts used in the simulation of the pre compensated system.

References

1. Tatarski, V. I., "Wave Propagation in a Turbulent Medium", p 170, Dover Publications, Inc., New York, 1961.
2. Fried, D. L., Evaluation of r_0 for Propagation Down Through the Atmosphere, Applied Optics, 13, 2620, 1974.
3. Goodman, J. W., "Introduction to Fourier Optics", p 85, McGraw Hill Company, San Francisco, 1968.
4. Harris, Sr., J. L., "Resolving Power and Decision Theory", J. Opt. Soc. Am. 54, 606, 1964.
5. _____, "Image Evaluation and Restoration", J. Opt. Soc. Am. 56, 569, 1966.
6. McGlamery, B. L., "Restoration of Turbulence Degraded Images", J. Opt. Soc. Am. 57, 293, 1967.
7. Helstrom, C. W., "Image Restoration by the Method of Least Squares", J. Opt. Soc. Am., 57, 297, 1967.
8. Babcock, H. W., "The Possibility of Compensating Astronomical Seeing", Astronomical Society of the Pacific, Vol. 65, No. 386, Oct. 1953.
9. Dyson, F. J., "Theory of Optical Image Improvement", Stanford Research Institute, Tech. report JSR-73-11., 1975.
10. Muller, R. A., and Buffington, A., J. Opt. Soc. Am. 64, 1200, 1974.
11. Wyant, J. C., Appl. Opt. 13, 200, 1974.